Modeling and detection of oil in sea water

Angeliki Xenaki[a)]
Department of Applied Mathematics and Computer Science, Technical University of Denmark, Kgs. Lyngby, 2800 Denmark

Peter Gerstoft
Scripps Institution of Oceanography, University of California San Diego, La Jolla, California 92093-0238

Klaus Mosegaard
Department of Applied Mathematics and Computer Science, Technical University of Denmark, Kgs. Lyngby, 2800 Denmark

(Received 15 April 2013; revised 19 July 2013; accepted 6 August 2013)

The challenge of a deep-water oil leak is that a significant quantity of oil remains in the water column and possibly changes properties. There is a need to quantify the oil settled within the water column and determine its physical properties to assist in the oil recovery. There are currently no methods to map acoustically submerged oil in the sea. In this paper, high-frequency acoustic methods are proposed to localize the oil polluted area and characterize the parameters of its spatial covariance, i.e., variance and correlation. A model is implemented to study the underlying mechanisms of backscattering due to spatial heterogeneity of the medium and predict backscattering returns. An algorithm for synthetically generating stationary, Gaussian random fields is introduced which provides great flexibility in implementing the physical model of an inhomogeneous field with spatial covariance. A method for inference of spatial covariance parameters is proposed to describe the scattering field in terms of its second-order statistics from the backscattered returns. The results indicate that high-frequency acoustic methods not only are suitable for large-scale detection of oil contamination in the water column but also allow inference of the spatial covariance parameters resulting in a statistical description of the oil field.
 [http://dx.doi.org/10.1121/1.4818897]

PACS number(s): 43.60.Fg, 43.60.Cg [ZHM] Pages: 2790–2798

I. INTRODUCTION

Prior to the oil accident of the Deepwater Horizon, the presence of oil in the sea was confined at shallow-water owing to either natural processes (e.g., biogenic oil) or human-induced pollution (e.g., oil slicks along shipping routes, blow outs from shallow water oil drills). Subsequently, the effort has been focused on monitoring and characterizing oil pollution on the sea surface. Remote sensing methods from satellites and aircrafts are efficient imaging methods of buoyant oil on the sea surface.[1,2] The challenge of a deep-water oil leak encountered in the case of the Deepwater Horizon is that a significant quantity of oil remained in the water column after the cease of the discharge from the wellhead[3,4] with serious environmental implications.[5–7] Much of the oil which was released into the water decomposed into stringy formations of viscous material which remained trapped, mixed with water, far below the sea surface;[3,4] see Fig. 1. Even though the mean values of the acoustic parameters, the compressibility, and density, of sea water and oil are approximately equal, weak scattering of acoustic waves (volume reverberation) can be observed in both areas due to random fluctuations of the acoustic parameters from their mean value. It is of interest to determine the physical properties of the new forms of oil and describe the spatial covariance of the submerged oil in order to monitor the degradation process.

Methods based on electromagnetic waves are inefficient for mapping submerged oil in the sea since the electromagnetic waves attenuate fast when traveling in water. Acoustic methods based on Doppler velocimetry which have been used[8,9] to quantify turbulent flow of hydrocarbons are inefficient to quantify the submerged oil since they require knowledge of the exact position of the oil leak. Tracking of the submerged oil is mainly based on fluorescence and dissolved oxygen measurements and low-frequency acoustic[1] or seismic methods.[10] These methods can detect submerged oil plumes but they do not provide information about the spatial distribution of the stringy oil contaminants in the water. High-frequency acoustic methods are promising since they can both overcome the optical opacity of the water and resolve the small-scale structure of the new forms of oil. Therefore, such methods can be used both to localize submerged oil fields and to characterize them in terms of their second order statistics.

The submerged oil in the water is modeled as a fluid medium with spatial heterogeneity, potentially exhibiting roughness at the interfaces with the water and possibly comprising inclusions of gas bubbles. Since the existence of submerged oil is controlled by the ambient density it is a reasonable assumption that the difference in the acoustic parameters between the two fluid media is small, producing weak scattering of the incident acoustic energy.[11,12]

[a)]Author to whom correspondence should be addressed. Current address: Scripps Institution of Oceanography, University of California San Diego, La Jolla, CA 92093-0238. Electronic mail: anxe@dtu.dk

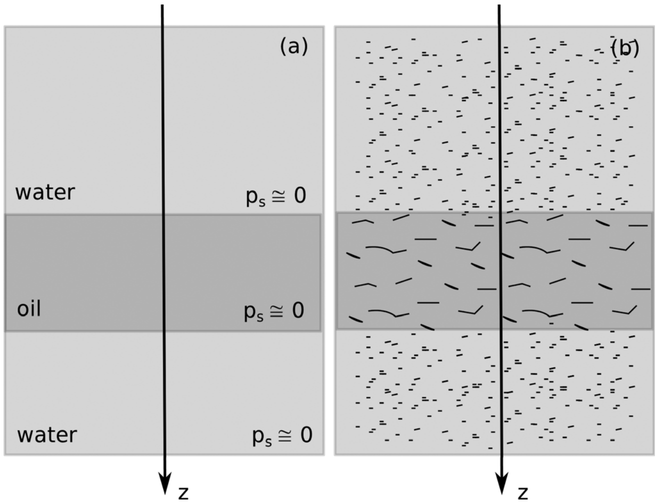

FIG. 1. Schematic for a submerged dispersed oil plume within the water column. (a) The mean values of the acoustic parameters for the two media are approximately equal. (b) Weak scattering can be observed due to random fluctuations of the acoustic parameters from their mean values.

Several authors[13–17] have used the weak scattering approach to model monostatic backscattering from inhomogeneous sediments in the seafloor. Palmese and Trucco[13] incorporate the effect of volume reverberation from the seabed to their model of imaging embedded objects with a three-dimensional (3D) monostatic sonar configuration. Li[14] and Li *et al.*[15] model the monostatic backscattering from 3D volume inhomogeneities in shallow water ocean sediments.

Tang[16] and Ivakin[17] developed independently the theoretical framework for a unified approach to describe weak scattering due to interface roughness and volume inhomogeneities, i.e., spatial fluctuations of the compressibility and density, from ocean sediments. The unified approach is based on the assumption that the roughness can be described as a specific kind of spatial fluctuation around an otherwise horizontal interface. Ivakin[17] further assumes that the weak scattering approach is not restricted to small-scale roughness but it extends to arbitrary roughness as long as the difference in the parameters between the adjacent media is not large. The unified approach in modeling scattering from irregular media facilitates the description of cases where the effect of volume and surface scattering is comparable and potentially coherent.

In this paper the weak scattering approach is applied for modeling the backscattered returns from inhomogeneous substances in the water column. A random field generator is introduced to implement a physical model of the inhomogeneous media and high-frequency active sonar is selected to collect the backscattered returns. Relative to methods used in ocean acoustics,[14,15] the random field generator[18] allows local perturbations of the modeled random field.

It is shown that high-frequency acoustics can be used to detect the submerged field and infer the parameters of its spatial covariance. Traditional methods describe weak scattering fields by comparing the statistical distribution of backscattering strength with known models.[12,19,20] An alternative method is proposed which allows the description of a stationary scattering field in terms of its second-order statistics without prior knowledge of its spatial covariance.

II. SCATTERING FROM INHOMOGENEITIES

Since the focus of this work is on modeling volume scattering, we undertake the derivation of the scattered pressure due to a region R in the medium with spatial heterogeneity in the acoustic parameters. The derivation follows the analysis by Morse and Ingard.[21]

Assuming time-stationarity, the Helmholtz equation for the scattered acoustic pressure p due to inhomogeneities in the acoustic parameters is given by

$$\nabla^2 p + k^2 p = -k^2\,\epsilon_\kappa(\mathbf{r})p - \mathrm{div}\,(\epsilon_\rho(\mathbf{r})\mathrm{grad}\,p), \tag{1}$$

where $k = \omega/c$ is the wavenumber, $\omega = 2\pi f$ is the radial frequency, c is the speed of sound, and

$$\epsilon_\kappa = \begin{cases} \dfrac{\kappa_e - \kappa}{\kappa} & \text{inside R} \\ 0 & \text{outside R}, \end{cases} \quad \epsilon_\rho = \begin{cases} \dfrac{\rho_e - \rho}{\rho_e} & \text{inside R} \\ 0 & \text{outside R} \end{cases}$$

are the deviations of the model parameters, namely, of the compressibility and density, relative to their unperturbed mean values, κ and ρ, respectively. The fluctuations vary in a statistical manner as a function of space.

Applying the Gauss-Green theorem, the Helmholtz equation takes the form of the integral equation,

$$\begin{aligned} p(\mathbf{r}_0) &= p_i(\mathbf{r}_0) \\ &\quad + \int_R (k^2\epsilon_\kappa(\mathbf{r})p(\mathbf{r}) - \nabla(\epsilon_\rho(\mathbf{r})\nabla p(\mathbf{r})))\,g(\mathbf{r}_0|\mathbf{r})\mathrm{d}\mathbf{r} \\ &= p_i(\mathbf{r}_0) + \int_R (k^2\epsilon_\kappa p g + \epsilon_\rho \nabla p \nabla g)\mathrm{d}\mathbf{r}, \end{aligned} \tag{2}$$

where g is the Green's function and p_i is the incident wave. The Green's function describes the sound pressure at an observation point $\mathbf{r}_0$ due to a point source located at $\mathbf{r}$ and is given by

$$g(\mathbf{r}_0|\mathbf{r}) = \frac{1}{4\pi|\mathbf{r}_0 - \mathbf{r}|} e^{-ik|\mathbf{r}_0 - \mathbf{r}|}. \tag{3}$$

The time convention $e^{i\omega t}$ is implied and neglected for simplicity. For far field radiation the Green's function takes the form in Eq. (4), where $r = |\mathbf{r}|$,

$$g(\mathbf{r}_0|\mathbf{r}) = \frac{1}{4\pi r} e^{-ik|\mathbf{r}_0 - \mathbf{r}|}. \tag{4}$$

The incident wave insonifies the region R. It emanates from a monopole located at the origin of the coordinate system out of the scattering region R and is given by Eq. (5),

$$p_i(\mathbf{r}) = A\frac{e^{-ikr}}{r}, \tag{5}$$

where A is the pressure amplitude at a distance 1 m from the source, k is the wavenumber of the incident wave, and r denotes the location of the insonified point.

The integral equation, Eq. (2), is exact and valid universally for parameter perturbations of arbitrary size.

Discontinuous perturbation can also be handled with Eq. (2) since it does not involve gradients of the model parameters.[17] Nevertheless, solving Eq. (2) requires exact expressions of the Green's function and the sound pressure inside the scattering region R. The integral equation for the scattered wave can be solved analytically only for a few special cases (e.g., scattering by spheres). Alternatively it can be solved by variational methods or approximations.[21,22]

In the case of weak scattering, first-order scattering is assumed, thus Born's approximation is applied. Born's approximation implies that the sound pressure inside the scattering region is equal to the incident sound pressure neglecting the effect of higher-order scattering.[21,22]

The sound pressure observed at a remote position $\mathbf{r}_0$ due to scattering from inhomogeneities in the acoustic parameters located at $\mathbf{r}$ within a region R is determined by inserting Eqs. (4) and (5) into Eq. (2). In a monostatic configuration and assuming that the Born approximation is valid the scattered sound pressure is given by[21]

$$p_s(\mathbf{r}_0) = \frac{k^2 A}{4\pi} \int_R \left((\epsilon_\kappa(\mathbf{r}) - \epsilon_\rho(\mathbf{r})) \frac{e^{-ik(|\mathbf{r}_0 - \mathbf{r}| + r)}}{r^2} \right) \mathrm{d}\mathbf{r}. \tag{6}$$

III. RANDOM FIELD GENERATOR

There are indications that the submerged oil extends throughout the water column as elongated formations of viscous material mixed with water and possibly with biological material.[3] Since the spatial distribution of scatterers due to dispersed oil varies in a complex way it is reasonable to model it as a random field of compressibility and density perturbations of the background medium with specified statistical properties.

In the absence of turbulence and for a short measurement interval, the random field is assumed to be spatially stationary and time-invariant. Stationarity can be exploited to develop a numerical method for synthetically generating random fields.

A. Methods for generating random fields

The term random field generator refers to an algorithm which utilizes uncorrelated normally distributed random numbers to generate more complex random fields with specific spatial covariance characteristics.[18,23,24] In principle, the algorithm generates a stationary random field, ε, by adding a convolution of a random Gaussian field, n, with a decomposition of the underlying covariance function, w, to the mean value, m,

$$\epsilon = m + w * n. \tag{7}$$

Several statistical methods have been proposed for synthetically generating random fields which differ in the implementation of the convolution in Eq. (7). Using the Cholesky decomposition of the covariance matrix,[25,26] the convolution is calculated by multiplying the lower triangular matrix by a vector of random uncorrelated numbers. The moving average (MA) method[27,28] offers an alternative implementation of the covariance decomposition. In this method, the covariance function is expressed as a convolution product of two mirror symmetric functions. The function resulting from the decomposition of the covariance function is further convolved with a set of uncorrelated random numbers on the field grid. The drawback of this method is that it is generally difficult to determine the decomposition function.[18,27,28]

Spectral methods perform the convolution in the spectral domain using the fast Fourier transform (FFT) algorithm.[14,15,23,24] The spectral methods are based on the fact that, for a stationary random field, the Fourier transform connects the covariance function, $C(\mathbf{h})$, with its spectral equivalent, the power spectrum, $S(\mathbf{k})$, where $\mathbf{h}$ and $\mathbf{k}$ are vectors denoting the lag and spectral distance, respectively,[29,30]

$$\begin{aligned} C(\mathbf{h}) &= \langle \epsilon(\mathbf{r}) \epsilon(\mathbf{r} + \mathbf{h}) \rangle \\ S(\mathbf{k}) &= \int_{-\infty}^{\infty} C(\mathrm{h}) e^{-i2\pi \mathbf{kh}} \, \mathrm{d}\mathbf{h}. \end{aligned} \tag{8}$$

Since a convolution in the spatial domain is equivalent to a product in the spectral domain and the Fourier transform of a real and even function is also a real and even function, the decomposition of the power spectrum is symmetric and can be calculated by its square root. Thus, the spectral methods generate random fields subject to specific covariance characteristics by multiplying the square root of the power spectrum by a set of complex Gaussian numbers, $N \sim \mathcal{CN}(0, 1)$, where $\mathcal{CN}(0, 1)$ denotes the standard complex normal distribution. Spectral methods perform the computations efficiently due to the FFT algorithm. However, equidistant grids are required. Besides, care should be taken on the selection of the random numbers generated in the spectral domain to obtain real-valued fields in the spatial domain.[14,15,18,23,24]

B. The FFT-MA generator

The numerical method used herein to generate discrete, stationary, random fields for the perturbations is called the fast Fourier transform-moving average (FFT-MA).[18] The FFT-MA method combines the advantages of the spectral methods and of the MA approach. It performs the computations in the spectral domain using the efficient FFT algorithm while preserving the generation of the random numbers in the spatial domain as in the MA framework,

$$\epsilon(\mathbf{r}) = m(\mathbf{r}) + F^{-1}\left\{ \sqrt{S(\mathbf{k})} F\{n(\mathbf{r})\} \right\}. \tag{9}$$

Briefly, the steps of the FFT-MA random field generator algorithm involve:

(1) Calculation of the discrete covariance function $C(\mathbf{h})$ on a spatial grid with spacing at least half of the characteristic length in each direction; see Sec. III C. It is important to perform the discretization symmetrically to obtain a real and even covariance function. Zero-padding at least to the extent of a characteristic length is required to avoid wrap-around effects.

(2) Generation of Gaussian random numbers from the standard normal distribution on the spatial grid $n(\mathbf{r}) \sim \mathcal{N}(0, 1)$.

(3) Fourier transform $C(\mathbf{h})$ and $n(\mathbf{r})$ to obtain the power spectrum $S(\mathbf{k})$ and the spectral representation of the random numbers $N(\mathbf{k})$, respectively. Since $C(\mathbf{h})$ is real and even, $S(\mathbf{k})$ is real and even as well.
(4) Computation of the square root of the power spectral density as in spectral methods $G(\mathbf{k}) = \sqrt{S(\mathbf{k})}$.
(5) Inverse Fourier transforms the product $G(\mathbf{k})N(\mathbf{k})$ giving the convolution product $g(\mathbf{r}) * n(\mathbf{r})$.
(6) Generation of the random field $\epsilon(\mathbf{r}) = m(\mathbf{r}) + g(\mathbf{r}) * n(\mathbf{r})$ according to the MA framework.

Compared to spectral methods the generation of the random numbers in the spatial domain allows local perturbations which will practically affect the field values on the grid to the extent of the correlation length. This is not possible in spectral methods where changing a random number in the spectral domain affects the whole spatial domain. Similar to the spectral methods, the FFT-MA algorithm requires regular grids in each direction (i.e., equidistant spacing) in the spatial domain.

C. Covariance models

The implemented FFT-MA algorithm can generate one-dimensional (1D), two-dimensional (2D), or 3D random fields with a Gaussian, Eq. (10), exponential, Eq. (11), or spherical, Eq. (12), covariance,[31,32]

$$C(h) = \sigma^2 e^{-3h^2/l^2}, \tag{10}$$

$$C(h) = \sigma^2 e^{-3h/l}, \tag{11}$$

$$C(h) = \begin{cases} \sigma^2\left(1 - \left(\dfrac{3}{2}\dfrac{h}{l} - \dfrac{1}{2}\left(\dfrac{h}{l}\right)^3\right)\right) & \text{if } h \le l \\ 0 & \text{if } h > l, \end{cases} \tag{12}$$

where $h = |\mathbf{h}|$ is the lag distance (isotropic case), $\sigma^2 = C(0)$ is the variance, and l is the characteristic length. The spherical covariance function becomes zero at a distance equal to the characteristic length. The Gaussian and exponential covariance functions reach the zero value asymptotically and have decayed by 95% at a distance equal to the characteristic length.

Figure 2 compares the three covariance models in the isotropic case. For short lag distances near the origin the Gaussian model has a parabolic behavior, suitable for modeling regular phenomena due to the smooth decay, while the exponential and the spherical model decay linearly.[32]

In the multidimensional case, the implemented FFT-MA algorithm can generate fields with geometric anisotropy as well.[31] In this case, the characteristic length is direction-dependent. A linear coordinate transformation involving a rotation and a scaling is used to include anisotropy in the expressions of Eqs. (10)–(12).[32]

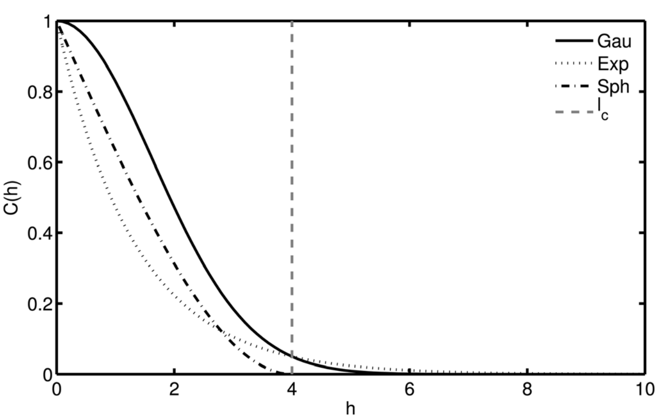

FIG. 2. 1D Gaussian (full line), exponential (dotted line), and spherical (dashed line) covariance functions as a function of the lag distance h. The variance is $\sigma^2 = 1$ and the characteristic length is $l = 4$.

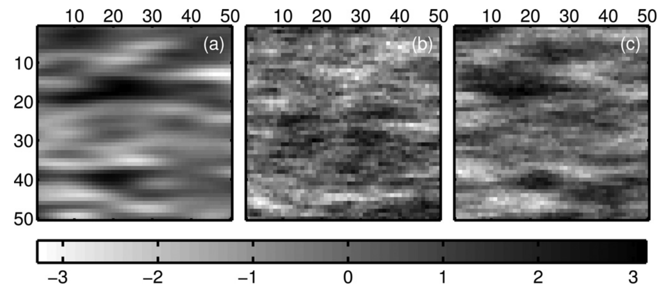

FIG. 3. Realizations of 2D anisotropic random fields with (a) Gaussian, (b) exponential, and (c) spherical covariance on a grid of 50×50 pixels. The mean field is $m = 0$ with variance $\sigma^2 = 1$, major characteristic length $l_{\max} = 20$ pixels in the horizontal direction and anisotropy factor (the ratio of the minor to the major characteristic length) 0.2 for all models.

D. Examples

A variety of covariance models can be used to determine the spatial properties of the generated field. In modeling this gives flexibility in representing different qualities of the field as smoothness or irregularity, isotropy or anisotropy. Figure 3 shows realizations of 2D anisotropic random fields with Gaussian, exponential, and spherical covariance. The field with a Gaussian covariance exhibits smooth characteristics while the field with an exponential covariance is more irregular.

The random numbers and the covariance parameters are dissociated and can be altered either separately or simultaneously. This is possible since the generating field is Gaussian and the resulting field is a linear transformation of the Gaussian field. The separation of the random and covariance parameters gives great flexibility which is useful for inverse methods. Figure 4 shows realizations of 2D anisotropic fields with Gaussian covariance generated by retaining the set of random numbers and altering the characteristic length. As the

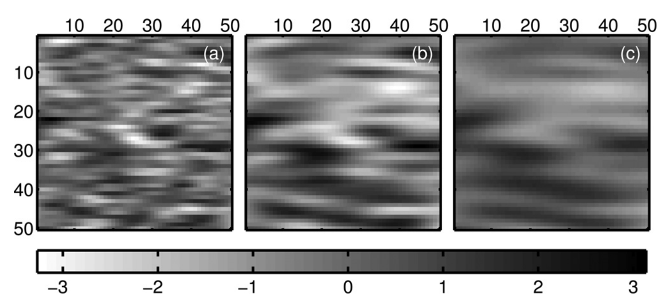

FIG. 4. Perturbation of covariance parameters only. Realizations of 2D anisotropic random fields with Gaussian covariance on a grid of 50×50 pixels. The mean field is $m = 0$ with variance $\sigma^2 = 1$ and anisotropy factor 0.2 in all cases. The major characteristic length is occurring in the horizontal direction and is (a) $l_{\max} = 10$, (b) $l_{\max} = 20$, and (c) $l_{\max} = 30$ pixels.

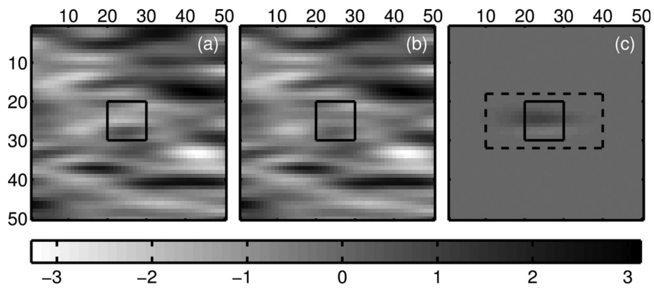

FIG. 5. Local alteration of the random numbers. (a) and (b) realizations of 2D anisotropic random fields with Gaussian covariance, mean $m = 0$, variance $\sigma^2 = 1$, major characteristic length $l_{\max} = 20$ pixels in the horizontal direction and anisotropy factor 0.2. The realization in (b) is generated by the same set of random numbers except from a window of 10×10 pixels (black square) where the random numbers are locally perturbed. (c) The difference between the realizations in (a) and (b). The region of perturbation augmented by the characteristic length in each direction is marked with a dashed rectangle.

characteristic length increases the spatial features are merged to larger formations but they appear at the same location.

The ability not only to alter the set of random numbers separately from the covariance parameters but also to perform local alterations is the main improvement of the FFT-MA algorithm with respect to spectral methods. This is due to the generation of random numbers in the spatial domain. Figure 5 exhibits the effect of a local alteration of the random set.

In conclusion, the FFT-MA algorithm provides an efficient and flexible method for implementing physical models of random fields.

IV. MODELING AND DETECTION OF VOLUME INHOMOGENEITIES

The random field generator and the propagation model are the necessary tools in simulating backscattered returns from weak scatterers. After choosing a receiving configuration, the backscattered returns are post-processed using beamforming to localize the scattering region from the received signals.

Active sensing (i.e., a pulse is used to insonify the area of interest) and a monostatic configuration (i.e., the transmitter and the receiver array are collocated) are considered here. A multibeam sonar is chosen as the transmitting and receiving configuration.

Following the specifications in Ref. 33, the considered transmitter emits a 200 kHz narrowband sinusoidal signal. The pulse is gated with a Hamming window of 120 μs length incorporating 24 periods. The duration of the transmitted pulse, T_s, dictates the range resolution, $\Delta r = cT_s/2$. The source level is 200 dB re 1 μPa at 1 m. The transmitter has a directivity pattern characterized by constant response within an angle of 140° in the across-track plane and a much narrower opening angle of 2° in the along-track plane.

The receiver comprises $N_m = 256$ hydrophones arranged in a uniform linear array (ULA) with $d_m = 1.6$ mm spacing. Delay-and-sum beamforming with Hamming weighting is applied[34] to impose directivity to the receiving array. The sound speed profile is assumed constant. The half-power beam width defines the angular resolution of the beamformer. The beam width at broadside is $\sin^{-1}[0.886(\lambda/N_m d_m)] \approx 1^\circ$ with uniform weighting[34] and 1.4° with Hamming weighting. Even though Hamming weighting degrades the angular resolution of the beamformer, it is chosen since it significantly suppresses the maximum sidelobe level from -13 dB with uniform weighting to -43 dB.

Sound attenuation due to dissipation in sea water is accounted for by introducing an imaginary part to the acoustic wavenumber.[11] The absorption coefficient is calculated according to the Francois-Garrison equation.[35,36] The attenuation is attributed to absorption from pure water and from the chemical relaxation of magnesium sulfate which is the main absorption mechanism at frequencies within the range of 10 to 500 kHz. The absorption coefficient is $\alpha = 50$ dB/km for salinity 35 ppm, temperature 6°, pH 8, depth 50 m, and frequency 200 kHz, corresponding to a sound speed of 1470 m/s. Even though the absorption for the oil contaminants is expected to be larger, the excess of attenuation is neglected since the sound propagates mainly into sea water.

Dynamic focusing is considered to relate the focusing distance with the travel time ($r = ct/2$), resulting in an infinite depth of field.[37,38] Time-varied gain (TVG) is applied to compensate for spreading loss and absorption making the received signals independent of the scatterer's distance. This corresponds to multiplication of the received signals, p_r, with a range dependent function $f(r) = r^2 e^{\alpha 2r}$. In the presence of additive ambient noise, $p_r = p_s + n$, the application of TVG to the received signals is expected to amplify not only the signal, the scattered pressure p_s, but also the noise with increasing range. Nevertheless, ambient noise is neglected since the scattered pressure, Eq. (6), is much higher than additive noise in the received signal due to the high source level and the high-frequency considered.

Since the transmitter of the sonar has a narrow directivity pattern in the along-track plane, only the 2D across-track plane is modeled. The model grid extends horizontally from $x = -100$ to 100 m and vertically from $z = 0.5$ to 100 m with spacing $dx = dz = 0.05$ m in both directions. The beamforming grid spans from $\theta = -70^\circ$ to 70° with spacing $d\theta = 1.4^\circ$ and from $r = 0.5$ to 100 m radially with spacing $dr = 0.1$ m. A range dependent correction, $1/rd\theta dr$, is applied to the reconstructed values on the beamforming grid to compensate for the increasing width of the grid cells with increasing range. The beamformer values are interpolated to the model grid after the reconstruction. The resolution cells become wider as the $|x|$ and z values increase resulting in lower resolution for distant locations. The range resolution is constant and equal to 0.1 m.

For acquiring a 3D image, a planar array is required, increasing the complexity of the processing. In this case sparse arrays is an option.[39]

A. Volume heterogeneity

A 2D field of volume inhomogeneities is considered representing the water column with a region of contamination characterized by a different covariance structure than the rest of the field.[3] The average compressibility and density are constant throughout the field.

It is often assumed that the compressibility fluctuations are proportional to density fluctuations with a position-independent proportionality factor.[19] Besides, compressibility fluctuations are larger than density fluctuations in fluids.[22] Therefore, only compressibility fluctuations are considered in the model of volume reverberation.

The selection of the parameters is somehow arbitrary due to lack of experimental information. For the pure water region an isotropic Gaussian covariance model [Eq. (10)] is selected with variance $\sigma_\kappa^2 = 0.001$ and characteristic length $l = 0.1$ m. The contaminated region is expected to have a higher viscosity and present layering due to oil/water interface tension.[40] Therefore, an anisotropic spherical covariance model is selected for the contaminated region with variance $\sigma_\kappa^2 = 0.01$, major characteristic length $l_{\max} = 2$ m occurring in the horizontal direction and minor characteristic length $l_{\min} = 0.5$ m occurring in the vertical direction. Figures 6(a) and 6(b) show the insonified area and the beamformer output.

Figures 6(c) and 6(d) show another case where the inhomogeneous fields in the two regions differ only in the characteristic lengths. Namely, the pure water region is described by an isotropic Gaussian covariance model with variance $\sigma_\kappa^2 = 0.01$ and characteristic length $l = 0.1$ m. The contaminated region is described by an anisotropic Gaussian covariance model with variance $\sigma_\kappa^2 = 0.01$, major characteristic length $l_{\max} = 2$ m occurring in the horizontal direction and minor characteristic length $l_{\min} = 0.5$ m occurring in the vertical direction.

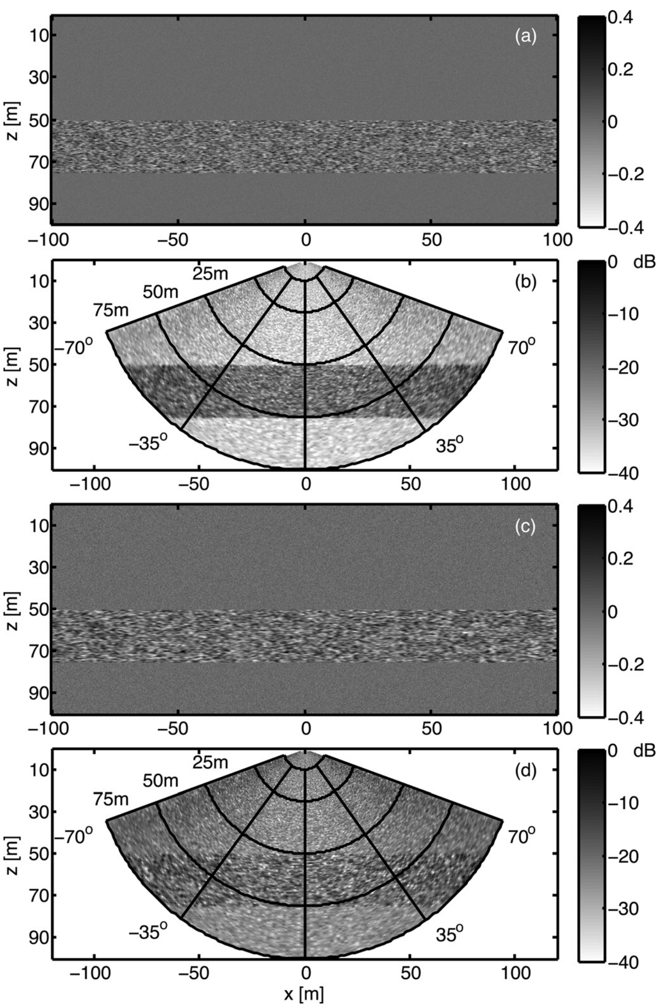

FIG. 6. (a) and (c) 2D fields of compressibility fluctuations in the water column and (b) and (d) the corresponding beamforming reconstructions. The contamination extends over 50 to 75 m depth characterized by a different covariance structure than the rest of the field. (c) and (d) The two fields differ only in the characteristic lengths.

B. Surface roughness

Based on the unified formulation[16,17] scattering from surface roughness is modeled as a special case of spatial heterogeneity. Equation (6) is used to calculate the scattered pressure attributed to surface roughness. In this case the covariance characteristics of the roughness at the interfaces are described by a 1D Gaussian covariance model with a variance of $\sigma^2 = 0.01$ and a characteristic length of $l = 0.1$ m.

Figure 7 shows the insonified area in the case of two distinct anomalous interfaces and the beamformer output.

C. Small gas bubbles

Exact formulas can be derived for the scattered pressure from spheres owing to their simple geometry. When the wavelength is long relative to the diameter of the sphere, the Born approximation is valid and the expressions can be simplified for simple scattering. The focus here is on light compressible spheres like gas bubbles in water or oil, for which the compressibility is larger, $\kappa_g > \kappa$, and the density is much smaller, $\rho_g \ll \rho$, than the corresponding values of the ambient fluid. Following Ref. 21, the scattered pressure at $\mathbf{r}_0$ due to a gas sphere at $\mathbf{r}$ with radius a smaller than the wavelength of the insonifying wave is approximated by

$$p_s(\mathbf{r}_0) = A\frac{e^{ikr}}{r}\left(\frac{1}{3}k^2a^3\left(\frac{\kappa_g}{\kappa}+3\right)\right). \tag{13}$$

Figure 8 shows the beamformed backscattered returns from 10^3 bubbles with radius $a = 0.5$ mm randomly distributed within the observation grid. The ratio of compressibilities is $\kappa_g/\kappa = 10^4$ since the compressibility of water is on

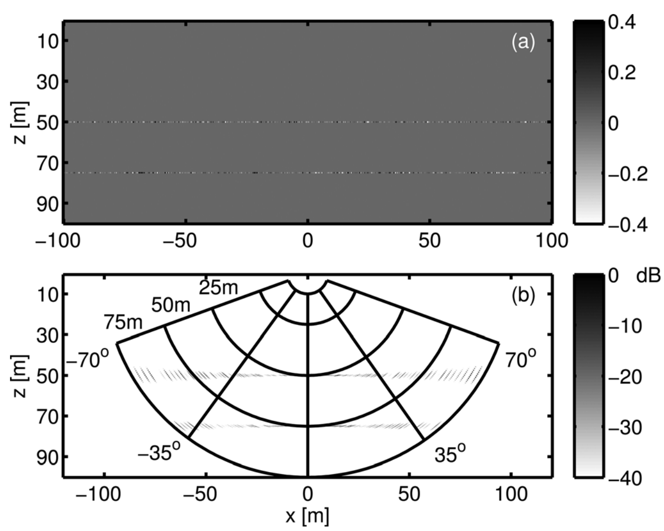

FIG. 7. (a) 2D field with two rough surfaces at 50 and 75 m, respectively, and (b) the beamforming reconstruction.

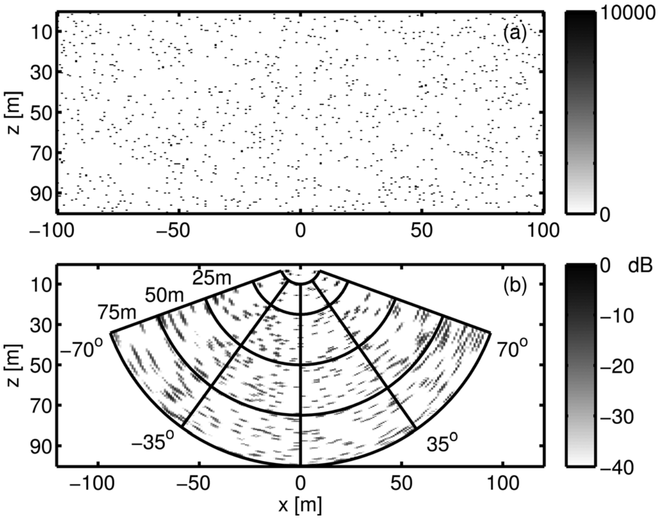

FIG. 8. (a) 2D field with randomly distributed small gas bubbles and (b) the beamforming reconstruction.

the order of $\kappa \simeq 10^{-10}$ Pa^{-1} and of air is on the order of $\kappa_g \simeq 10^{-6}$ Pa^{-1}.

V. INFERENCE OF SPATIAL COVARIANCE PARAMETERS

In an acoustic backscattering model of volume inhomogeneities, a statistical description of the field is more appropriate than a deterministic description due to the complex structure of the inhomogeneities.[30,41] Besides, a deterministic description of the field has less to offer when the interest is in studying volume reverberation in a medium where there is flow, such as in the water column.

Typically, volume reverberation is described by the statistical distribution of the backscattering strength. The backscattering strength is defined as the ratio of the scattered intensity to the incident intensity per unit volume in dB.[11,12,30,42,43] This measure is widely used in sonar applications concerned with target detection and identification[44,45] or with the remote classification of weak scattering mechanisms such as seafloor sedimentation by comparison to known models.[12,19,20] The backscattering strength is proportional to the cross spectral density thus related to the statistical properties of the field.[20,44,46] However, for narrowband measurements the backscattering strength provides a single measure and additional information for covariance parameters are required to relate the spatial variation of the scattering field to a covariance model. Herein, an alternative method is proposed to infer the covariance parameters of the scattering field directly from the beamforming reconstruction without using prior knowledge on the spatial covariance.

Using the Fraunhofer approximation, the range in the phase term of the far field expression of the Green's function [Eq. (4)] can be approximated by the first-order terms of a second-order binomial expansion,[37]

$$|\mathbf{r}_0 - \mathbf{r}| \approx r - \hat{\mathbf{r}} \cdot \mathbf{r}_0, \tag{14}$$

where $r = |\mathbf{r}|$ and $\hat{\mathbf{r}} = \mathbf{r}/r$ is the unit vector in the direction of the scatterer's location.

After application of dynamic focusing and TVG (compensating for the r^2 attenuation term), the signals received at the horizontal sensor locations, $\mathbf{x}_q = [\mathbf{q} - (N_m - 1/2)]d_m$, $\mathbf{q} = [0, 1, ..., N_m - 1]$, according to Eq. (6) are

$$\begin{aligned}\mathbf{p}_q(r) &\propto \sum_\theta \epsilon_\kappa(\theta, r) e^{-ik(2r - \mathbf{x}_q \sin(\theta))} \\ &\propto e^{-ik2r} \sum_\theta \epsilon_\kappa(\theta, r)\mathbf{v}(\theta),\end{aligned} \tag{15}$$

where r is the radial distance of focus and $\mathbf{v}(\theta) = e^{ik\mathbf{x}_q \sin(\theta)}$.

Applying conventional beamforming with Hamming weighting to the received signals, the beam associated with the steering angle θ_f at radial distance r is

$$b_f(\theta_f, r) = (\mathbf{w}_H \odot \mathbf{v}(\theta_f))^\dagger \cdot \mathbf{p}_q(r), \tag{16}$$

where $\mathbf{w}_H$ is the vector of the Hamming weights, † denotes conjugate transpose, and $\odot$ denotes element-wise multiplication.

Introducing the beam pattern as a function of the arrival angle θ when the array is steered at θ_f,[34]

$$B_H(\theta, \theta_f) = (\mathbf{w}_H \odot \mathbf{v}(\theta_f))^\dagger \cdot \mathbf{v}(\theta), \tag{17}$$

the beam $b_f(\theta_f, r)$ is expressed as

$$b_f(\theta_f, r) = e^{-ik2r} \sum_\theta \epsilon_\kappa(\theta, r) B_H(\theta, \theta_f). \tag{18}$$

Thus the beamformer output normalized by the maximum value in the beamforming reconstruction is connected to the field values as

$$b_{\text{out}}(\theta_f, r) = \frac{\left|\sum_\theta \epsilon_\kappa(\theta, r) B_H(\theta, \theta_f)\right|^2}{\max_{(\theta_f, r)} \left|\sum_\theta \epsilon_\kappa(\theta, r) B_H(\theta, \theta_f)\right|^2} \tag{19}$$

or

$$b(\theta_f, r) = \sqrt{b_{\text{out}}} = \frac{\left|\sum_\theta \epsilon_\kappa(\theta, r) B_H(\theta, \theta_f)\right|}{\max_{(\theta_f, r)} \left|\sum_\theta \epsilon_\kappa(\theta, r) B_H(\theta, \theta_f)\right|}. \tag{20}$$

According to Eq. (20), the square root of the beamformer output at a point on the beamforming grid contains the contribution of all the field values on the radial distance of focus, $\epsilon_\kappa(\theta, r)$, weighted by the beam pattern. However, the more the beam pattern resembles a delta function, the more the square root of the beamformer output, $b(\theta_f, r)$, will be proportional to the corresponding field value, $\epsilon_\kappa(\theta_f, r)$. Thus, the parameters of the spatial covariance of a field of volume inhomogeneities can be estimated by the statistics of the square root of the beamforming output.

For a stationary random process, u, the discrete spatial covariance function can be estimated from a finite number of samples, N, as[47]

$$\hat{C}(\eta) = \frac{1}{N}\sum_{i=1}^{N-\eta}(u_{i+\eta} - \bar{u})(u_i - \bar{u}), \tag{21}$$

where $\eta = 0, 1, ..., N-1$, $\bar{u} = 1/N\sum_{i=1}^{N} u_i$ is the sample mean and denotes an estimate.

For a 2D field the sample covariance estimate is

$$\hat{C}(h_x, h_z) = \frac{1}{N_x}\frac{1}{N_z}\sum_{i=1}^{N_x-\xi}\sum_{j=1}^{N_z-\zeta}(b_c(x_i + h_x, z_j + h_z) - \bar{b}_c)(b_c(x_i, z_j) - \bar{b}_c), \tag{22}$$

where N_x, N_z denote the number of sample grid points in the x and z directions, dx, dz are the corresponding grid spacings, $\xi = 0, 1, ..., N_x - 1$, $\zeta = 0, 1, ..., N_z - 1$ and $h_x = \xi \mathrm{d}x$, $h_z = \zeta \mathrm{d}z$ are the lag distances in the x and z directions, respectively.

In order to obtain the beamformer values on the sample grid in Cartesian coordinates, $b_c(x, z)$, interpolation is used based on the nearest neighbor method.

Covariance sample estimates are calculated for the field in Fig. 6(b). The sampling window has dimensions $N_x \mathrm{d}x = 10\,\mathrm{m}$ ($\mathrm{d}x = 0.05\,\mathrm{m}$) in the x direction and $N_z \mathrm{d}z = 1\,\mathrm{m}$ ($\mathrm{d}z = 0.05\,\mathrm{m}$) in the z direction. The sampling window is chosen such that it exceeds the correlation lengths in each direction and that it is small enough to examine areas where the resolution cells have approximately the same size, thus fulfill the condition of spatial stationarity. Additional averaging over 20 beamforming reconstructions is used to improve the statistical estimate. Since the covariance is expected to be non-negative, only non-negative values are used.

Figures 9 and 10 show examples of covariance estimation when sampled at the contaminated region characterized by an anisotropic, spherical covariance model and at the sea water region characterized by an isotropic, Gaussian covariance model, respectively. The specific samples are centered to the grid where the beamformer resolution is 1.2 m in the x direction (due to beam width) and 0.1 m in the z direction (due to time-gating). Specifically, the sampling windows extend from -5 to 5 m in the x direction and from 52.5 to 53.5 m and 48.5 to 49.5 m, respectively, in the z direction. The theoretical [Figs. 9(a), 9(b), 10(a), and 10(b)] and estimated [Figs. 9(c), 9(d), 10(c), and 10(d)] covariance functions are compared in the direction both of the major and the minor characteristic length for the two fields. The variance corresponds to the maximum value of the covariance function at zero lag. The characteristic length corresponds to the lag where the covariance function has decayed by at least 95% and is denoted by a dashed line in each case.

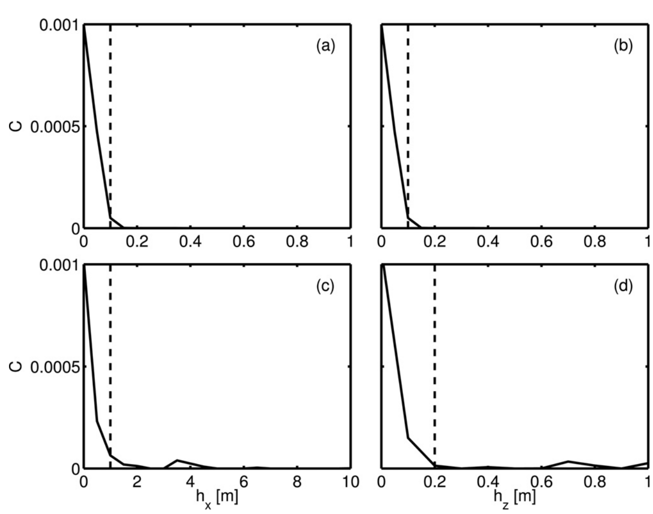

FIG. 9. (a) and (b) True and (c) and (d) reconstructed covariance function for the region characterized by an anisotropic, spherical covariance model with variance $\sigma_\kappa^2 = 0.01$, major characteristic length $l_{\max} = 2\,\mathrm{m}$ in the x direction and minor characteristic length $l_{\min} = 0.5\,\mathrm{m}$ in the z direction. The dashed lines denote the characteristic lengths in each case.

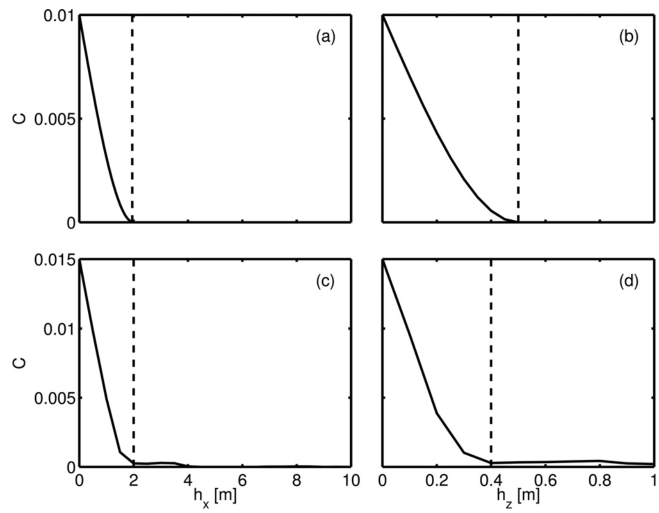

FIG. 10. (a) and (b) True and (c) and (d) reconstructed covariance function for the region characterized by an isotropic, Gaussian covariance model with variance $\sigma_\kappa^2 = 0.001$, and characteristic length $l = 0.1\,\mathrm{m}$. The dashed lines denote the characteristic lengths in each case.

For the contaminated region (Fig. 9) the sample covariance provides good estimates of the characteristic lengths in both directions since the characteristic lengths exceed the resolution. Contrary, at the sea-water region (Fig. 10) the characteristic length is smaller than the resolution in the x direction of the beamformer, thus the estimate does not reflect the actual values of the parameter but rather the resolution limits; note the scale difference on the h_x axis.

VI. CONCLUSION

Detection and characterization of submerged oil in the sea water is studied with a model of backscattering from volume inhomogeneities. The physical model for the submerged oil is represented as a random field of compressibility fluctuations which exhibits stationary spatial correlation. A random field generator based on the FFT-MA approach is introduced to implement the physical model. The proposed algorithm provides great flexibility in different modeling scenarios. An active, high-frequency, monostatic sonar is selected to insonify the medium and collect the backscattered returns. The random field is localized with beamforming and inference of spatial covariance is based on the statistics of the beamforming reconstruction.

The simulation results indicate that inference of the spatial covariance parameters is possible with high-frequency acoustics, providing a quantitative statistical description of the random field. Nevertheless, the reconstructions are subject to resolution limitations of the sonar. The use of high frequencies, resulting in narrow beam widths, improves the resolution and allows the detection of small scale characteristics. On the other hand, the use of high frequencies requires challenging sonar designs with high power demands, since high-frequency sound attenuates fast when propagating in the water, and small interelement spacing.

[1]R. L. Crout, "Measurements in support of the Deepwater Horizon (MC-252) oil spill response," in *Proceedings of SPIE8030, Ocean Sensing and Monitoring III*, Vol. 8030, International Society for Optics and Photonics, Orlando, FL (2011).

[2]L. Shi, A. Y. Ivanov, M. He, and C. Zhao, "Oil spill mapping in the western part of the East China Sea using synthetic aperture radar imagery," Int. J. Remote Sens. **29**, 6315–6329 (2008).

[3]M. Schrope, "Oil spill: Deep wounds," Nature **472**, 152–154 (2011).

[4]S. A. Socolofsky, E. E. Adams, and C. R. Sherwood, "Formation dynamics of subsurface hydrocarbon intrusions following the Deepwater Horizon blowout," Geophys. Res. Lett. **38**, 1–6 (2011).

[5]R. Camilli, C. Reddy, D. Yoerger, B. Van Mooy, M. Jakuba, J. Kinsey, C. McIntyre, S. Sylva, and J. Maloney, "Tracking hydrocarbon plume transport and biodegradation at Deepwater Horizon," Science **330**, 201–204 (2010).

[6]J. Kessler, D. Valentine, M. Redmond, M. Du, E. Chan, S. Mendes, E. Quiroz, C. Villanueva, S. Shusta, L. Werra, S. Yvon-Lewis, and T. Weber, "A persistent oxygen anomaly reveals the fate of spilled methane in the deep Gulf of Mexico," Science **331**, 312–315 (2011).

[7]A. Diercks, R. Highsmith, V. Asper, D. Joung, Z. Zhou, L. Guo, A. Shiller, S. Joye, A. Teske, N. Guinasso, T. Wade, and S. Lohrenz, "Characterization of subsurface polycyclic aromatic hydrocarbons at the Deepwater Horizon site," Geophys. Res. Lett. **37**, 1–6 (2010), doi:10.1029/2010GL045046.

[8]R. Camilli, D. Di Iorio, A. Bowen, C. M. Reddy, A. H. Techet, D. R. Yoerger, L. L. Whitcomb, J. S. Seewald, S. P. Sylva, and J. Fenwick, "Acoustic measurement of the Deepwater Horizon Macondo well flow rate," Proc. Natl. Acad. Sci. U.S.A. **109**, 20235–20239 (2012).

[9]M. K. K. McNutt, R. Camilli, T. J. Crone, G. D. Guthrie, P. A. Hsieh, T. B. Ryerson, O. Savas, and F. Shaffer, "Review of flow rate estimates of the Deepwater Horizon oil spill," Proc. Natl. Acad. Sci. U.S.A. **109**, 20260–20267 (2012).

[10]J. A. Hildebrand, L. Armi, and P. C. Henkart, "Seismic imaging of the water-column deep layer associated with the Deepwater Horizon oil spill," Geophysics **77**, 11–16 (2012).

[11]X. Lurton, *An Introduction to Underwater Acoustics: Principles and Applications* (Praxis Publishing, Chichester, UK, 2002).

[12]L. R. LeBlanc, S. G. Schock, D. L. DeBruin, M. Jenkins, and L. Munro, "High-resolution sonar volume scattering measurements in marine sediments," J. Acoust. Soc. Am. **97**, 2979–2986 (1995).

[13]M. Palmese and A. Trucco, "Acoustic imaging of underwater embedded objects: Signal simulation for three-dimensional sonar instrumentation," IEEE Trans. Instrum. Meas. **55**, 1339–1347 (2006).

[14]D. Li, "Modeling of monostatic bottom backscattering from three-dimensional volume inhomogeneities and comparisons with experimental data," Ph.D. dissertation, Massachusetts Institute of Technology, Cambridge, MA, 1997, pp. 17–186.

[15]D. Li, G. Frisk, and D. Tang, "Modeling of bottom backscattering from three-dimensional volume inhomogeneities and comparisons with experimental data," J. Acoust. Soc. Am. **109**, 1384–1397 (2001).

[16]D. Tang, "A note on scattering by a stack of rough interfaces," J. Acoust. Soc. Am. **99**, 1414–1418 (1996).

[17]A. Ivakin, "A unified approach to volume and roughness scattering," J. Acoust. Soc. Am. **103**, 827–837 (1998).

[18]M. L. Ravalec, B. Noetinger, and L. Y. Hu, "The FFT moving average (FFT-MA) generator: An efficient numerical method for generating and conditioning Gaussian simulations," Math. Geol. **32**, 701–723 (2000).

[19]D. R. Jackson, K. B. Briggs, and M. D. Richardson, "Tests of models for high-frequency seafloor backscatter," IEEE J. Ocean. Eng. **21**, 458–470 (1996).

[20]A. N. Gavrilov and I. M. Parnum, "Fluctuations of seafloor backscatter data from multibeam sonar systems," IEEE J. Ocean. Eng. **35**, 209–219 (2010).

[21]P. M. Morse and K. U. Ingard, *Theoretical Acoustics*, International Series in Pure and Applied Physics (McGraw-Hill, New York, 1968), Chap. 8.

[22]L. A. Chernov, *Wave Propagation in a Random Medium* (McGraw-Hill, New York, 1960), Chap. 4.

[23]M. J. L. Robin, A. L. Gutjahr, E. A. Sudicky, and J. L. Wilson, "Cross-correlated random field generation with the direct Fourier transform method," Water Resour. Res. **29**, 2385–2397 (1993), doi:10.1029/93WR00386.

[24]F. Ruan and D. McLaughlin, "An efficient multivariate random field generator using the fast Fourier transform." Adv. Water Resour. **21**, 385–399 (1998).

[25]F. Alabert, "The practice of fast conditional simulations through the LU decomposition of the covariance matrix," Math. Geol. **19**, 369–386 (1987).

[26]M. Davis, "Production of conditional simulations via the LU triangular decomposition of the covariance matrix," Math. Geol. **19**, 91–98 (1987).

[27]A. G. Journel, "Geostatistics for conditional simulation of ore bodies," Econ. Geol. **69**, 673–687 (1974).

[28]D. S. Oliver, "Moving averages for Gaussian simulation in two and three dimensions," Math. Geol. **27**, 939–960 (1995).

[29]J. Bendat and A. Piersol, *Random Data: Analysis and Measurement Procedures* (Wiley, Hoboken, NJ, 2011), Vol. 729, Chap. 5.

[30]D. R. Jackson and M. D. Richardson, *High-Frequency Seafloor Acoustics*, Monograph Series in Underwater Acoustics (Springer, New York, 2007), Chap. 2.

[31]T. M. Hansen, K. S. Cordua, M. C. Looms, and K. Mosegaard, "SIPPI: A MATLAB toolbox for sampling the solution to inverse problems with complex prior information: Part 1-Methodology," Comput. Geosci. **52**, 470–480 (2013).

[32]P. Goovaerts, *Geostatistics for Natural Resources Evaluation* (Oxford University Press, New York, 1997), Chap. 4.2.

[33]G. Wendelboe, H. Dahl, E. Maillard, and L. Bjorno, "Towards a fully calibrated multibeam echo sounder," in *Proceedings of Meetings on Acoustics*, Edinburgh, UK, 2012, Vol. 17, pp. 1836–1843.

[34]H. Van Trees, *Optimum Array Processing (Detection, Estimation, and Modulation Theory, Part IV)* (Wiley-Interscience, New York, 2002), Chaps. 2 and 3.

[35]R. E. Francois and G. R. Garrison, "Sound absorption based on ocean measurements. Part I: Pure water and magnesium sulfate contributions," J. Acoust. Soc. Am. **72**, 896–907 (1982).

[36]R. E. Francois and G. R. Garrison, "Sound absorption based on ocean measurements. Part II: Boric acid contribution and equation for total absorption," J. Acoust. Soc. Am. **72**, 1879–1890 (1982).

[37]V. Murino and A. Trucco, "Three-dimensional image generation and processing in underwater acoustic vision," Proc. IEEE **88**, 1903–1984 (2000).

[38]V. Murino and A. Trucco, "Underwater 3D imaging by FFT dynamic focusing beamforming," in *Proceedings of ICIP-94, IEEE International Conference*, Austin, TX (1994), Vol. 1, pp. 890–894.

[39]A. Trucco, M. Palmese, and S. Repetto, "Devising an affordable sonar system for underwater 3-D vision," IEEE Trans. Instrum. Meas. **57**, 2348–2354 (2008).

[40]P. De Gennes and C. Taupin, "Microemulsions and the flexibility of oil/water interfaces," J. Phys. Chem. **86**, 2294–2304 (1982).

[41]A. Turgut, "Inversion of bottom/subbottom statistical parameters from acoustic backscatter data," J. Acoust. Soc. Am. **102**, 833–852 (1997).

[42]A. N. Ivakin and J.-P. Sessarego, "High frequency broad band scattering from water-saturated granular sediments: Scaling effects," J. Acoust. Soc. Am. **122**, EL165–EL171 (2007).

[43]H. Medwin and C. S. Clay, *Fundamentals of Acoustical Oceanography* (Academic Press, Boston, 1998), Chap. 9.

[44]A. A. Douglas and A. P. Lyons, "Novel physical interpretations of K-distributed reverberation," IEEE J. Ocean. Eng. **27**, 800–813 (2002).

[45]A. P. Lyons and A. A. Douglas, "Statistical characterization of high-frequency shallow-water seafloor backscatter," J. Acoust. Soc. Am. **106**, 1307–1315 (1999).

[46]N. P. Chotiros, "Non-Rayleigh distributions in underwater acoustic reverberation in a patchy environment," IEEE J. Ocean. Eng. **35**, 236–241 (2010).

[47]G. M. Jenkins and D. G. Watts, *Spectral Analysis and its Applications* (Holden-Day, San Francisco, CA, 1968), Chap. 5, pp. 171–189.